



Aerodynamic Design and Analysis of the Hyperloop

James Braun,* Jorge Sousa,† and Cem Pekardan‡
Purdue University, West Lafayette, Indiana 47906

DOI: 10.2514/1.J055634

The Hyperloop vehicle is a conceptual mode of transportation in which a pod travels at high speed through a low-pressure tunnel to minimize the aerodynamic drag. In the current paper, an aerodynamic design procedure of the Hyperloop vehicle for a design competition on a half-scale track is proposed and developed. The design process consists of a preliminary one-dimensional analysis of the pod through a reduced-flow model followed by a differential evolution multi-objective optimization coupled with a two-dimensional computational-fluid-dynamics solver. Finally, the optimal and initial designs are evaluated with three-dimensional simulations. Two main aerodynamic design objectives were evaluated to explore different conceptual ideas. One design focused on the ability to generate a certain amount of lift to mitigate the responsibility of the main levitation system, whereas the second design targeted the minimization of the aerodynamic drag to reduce the propulsion requirements.

Nomenclature

A	=	area, m
C_f	=	skin friction
D	=	drag, N
d	=	particle hard-shell diameter, m
Kn	=	Knudsen number
k_b	=	Boltzmann constant, $\text{m}^2 \cdot \text{kg} \cdot \text{s}^{-2} \cdot \text{K}^{-1}$
L	=	lift, N
l	=	characteristic length, m
M	=	Mach number
\dot{m}	=	mass flow, $\text{kg} \cdot \text{s}^{-1}$
n	=	correlation number
P	=	pressure, Pa
P'	=	dimensionless pressure gradient
Re	=	Reynolds number; $U l / \nu$
S_p	=	dimensionless shear parameter
T	=	static temperature, K
U	=	velocity, $\text{m} \cdot \text{s}^{-1}$
x	=	distance, m
γ	=	heat capacity ratio
ν	=	kinematic viscosity, $\text{m}^2 \cdot \text{s}^{-1}$
τ	=	wall shear stress, Pa

Subscripts

e	=	edge of the boundary layer
W	=	wall
0	=	total quantities

I. Introduction

THERE is a continuous interest to reduce travel times between distant human settlements while improving the overall efficiency of the transportation system. Transportation for short distances can be particularly inefficient due to additional travel time at airports or train stations. In 2013, Musk [1] triggered the attention

of the engineering society by proposing the Hyperloop concept as an alternative mode of transportation, with benefits in terms of performance and comfort for traveling distances below 1500 km. A representation of a Hyperloop pod traveling in the tube can be seen in Fig. 1. The concept consists of a levitating vehicle/pod traveling at high speeds (~ 300 m/s), inside a low-pressure tube (~ 100 Pa) that minimizes aerodynamic drag. The levitation can be achieved through an air-bearings system that generates a smooth air cushion, although different methods such as magnetic levitation or rails can be explored, depending on the application and feasibility. In case of an air-bearing system, the required high-pressure air can be delivered by a compressor placed in front of the pod. Additionally, with this system, part of the flow can be compressed and bypass the throat area, which helps to delay the flow choking.

The Hyperloop shifts the design of the vehicle from a classical external aerodynamic problem, as typically found in airplanes, trains, and automobiles [2–4], to an internal aerodynamic perspective, which unveils new fluid dynamics challenges that need to be addressed in the design process. In 2015, Chin et al. [5] presented an overall system of the Hyperloop concept and quantified the choking risk, which is determined by the minimum section (throat) between the pod and the outer tube wall. In a full scale operation, the pod can reach transonic speeds, and because of the flow acceleration in the bypass region (between the tube and the pod), sonic speeds (choking) can be achieved. When this occurs, high-pressure blockage is generated in front of the pod, endangering the operability of this system. Furthermore, the low-pressure operation leads to low Reynolds numbers, which enhances the risk of early separation of a laminar boundary layer in rear part of the vehicle. Therefore, a detailed aerodynamic analysis is fundamental to complement ongoing commercial feasibility studies such as the ones presented by Decker et al. [6] and Taylor et al. [7].

In June 2015, Space Exploration Technologies (SpaceX) announced a student competition around the Hyperloop design [8] with the idea to engage participants to design and build pods that are tested in an experimental Hyperloop tube constructed in Los Angeles. The 1 mile track consists of a central T-shaped beam that could be used for guidance or levitation and an initial pusher plate to accelerate the pod. The sizing of the tube is intended to be half-scale of the tube in the Hyperloop Alpha proposal [1]. Furthermore, operating pressure of the tube can be selected by the teams, which enables the search for optimal operating pressures for each proposed design. In the competition, the design speed was up to 110 m/s [9].

Therefore, an aerodynamically efficient pod operating under optimized pressure levels is essential for success in this competition and future technological developments.

The present paper describes our proposed design approach that was tailored for the present competition. We developed a design tool of the pod through a reduced-flow model, which enabled us to quickly assess lift and drag for several operating conditions. This was used as baseline for a multi-objective optimization with

Presented as Paper 2016-4812 at the 52nd AIAA/SAE/ASEE Joint Propulsion Conference, Salt Lake City, Utah, 25–27 July 2016; received 28 August 2016; revision received 22 May 2017; accepted for publication 25 May 2017; published online 26 July 2017. Copyright © 2017 by James Braun, Jorge Sousa, and Cem Pekardan. Published by the American Institute of Aeronautics and Astronautics, Inc., with permission. All requests for copying and permission to reprint should be submitted to CCC at www.copyright.com; employ the ISSN 0001-1452 (print) or 1533-385X (online) to initiate your request. See also AIAA Rights and Permissions www.aiaa.org/randp.

*Graduate Student, Zucrow Laboratories, 500 Allison Road; jamesbraun91@gmail.com.

†Postdoctoral Researcher, Zucrow Laboratories, 500 Allison Road; jorge.f.sousa@gmail.com.

‡Graduate Student, 701 West Stadium Avenue; cpekarda@purdue.edu.

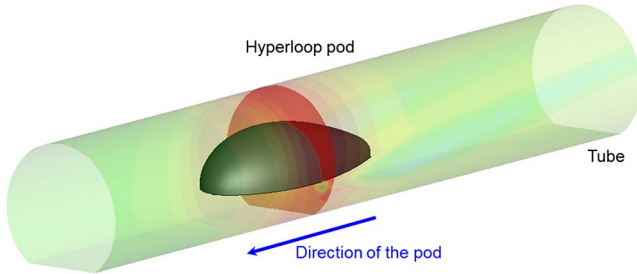


Fig. 1 Representation of a Hyperloop pod traveling in the tube.

two-dimensional (2-D) computational fluid dynamics (CFD) simulations. During the design process, we evaluated several aerodynamic design objectives to explore different conceptual ideas such as the maximization of lift and minimization of drag on the vehicle. Finally, those ideas were verified through three-dimensional (3-D) CFD simulations.

Some of the design ideas presented in this paper could be used to help the competing students to obtain a highly efficient and lightweight design in a timely manner. In this paper, the compressor was not considered due to the relatively low speed of the vehicle, the short distance, and the small size of the pod. However, the aerodynamic design philosophy can also be used as a path to develop a more detailed procedure involving other systems and to evaluate a full-scale Hyperloop system.

II. Methodology

A. Geometrical Definition and Design Space

The aerodynamic geometry of the pod is generated through a Bezier curve that ensures curvature continuity on the design (Fig. 2). The geometrical parameterization of the vehicle is achieved with several control points along the streamwise direction (blue crosses in Fig. 2). These points are free to move in the normal direction with

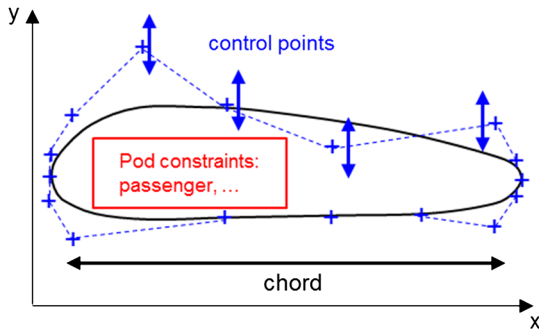


Fig. 2 Parameterization of the pod geometry through a Bezier curve, with a consequent representation of the design constraints.

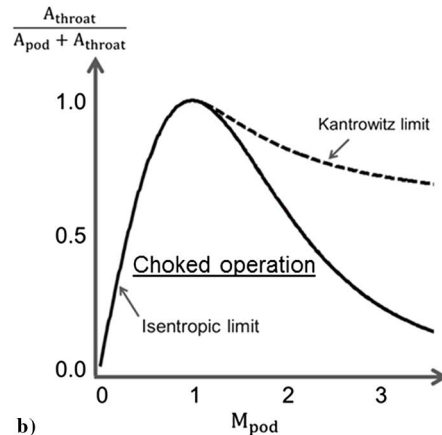
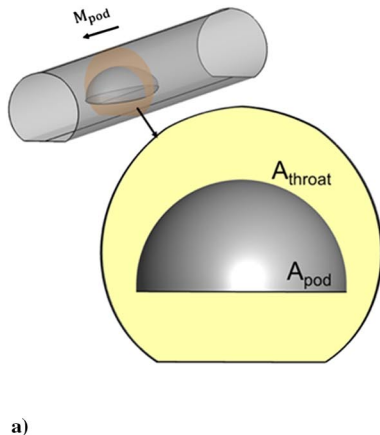


Fig. 3 a) Minimum sectional area of the tube and the area of the pod. b) Isentropic and Kantrowitz limit in function of the contraction area and Mach number of the pod.

respect to the flow. This allows for an automation of the design process that enables the creation of a pod shape within a very large design space. Additionally, a constraint checker verifies that all the internal pod subsystems (such as passenger, battery, etc.) fit within the aerodynamic geometry.

A fundamental aspect when dealing with internal transonic flow is the choking limitation. In subsonic operation, the Mach number increases with any area contraction until sonic conditions are achieved at the minimum sectional area, which we call the throat (A_{throat}). Because the mass flow is maximized when $M = 1$, the throat area bounds the maximum possible mass flow rate. Figure 3a illustrates the frontal area of the pod (A_{pod}) and the remaining area within the tunnel, which represents the throat area. Figure 3b depicts the different operating regimes as a function of the Mach number of the pod and the area ratio between the tunnel area and the throat area. The isentropic limit sets the points where sonic conditions are reached at the throat. For example, if the pod is traveling at a Mach number of 0.4, the throat area (A_{throat}) needs to be approximately 50% of the tunnel area to avoid choking. If we design the pod with such geometrical conditions and accelerate to a higher speed (moving toward the right in the plot), the throat would not be able to swallow the new mass flow, and consequently, pressure would build up upstream of the vehicle to ensure that the Mach number is 1 at the throat. In case of supersonic travel conditions, we would be bounded by a more restrictive limit known as the Kantrowitz limit [10,11], represented in Fig. 3b. Only if the area ratio would be high enough to satisfy the Kantrowitz limit, we could ensure a supersonic cruise velocity. Hence, it is necessary that our pod design is above the isentropic limit for subsonic operation or above the Kantrowitz limit for supersonic operations.

B. Flow Analysis

1. One-Dimensional Reduced-Flow Model: Viscous Correction

A first requirement for the design procedure is the knowledge of the flowfield model. Therefore, we need to verify if the continuum approach is suitable to solve the flowfield for the targeted operating conditions (for operating static pressures of 100 to 50 kPa). Hence, it is necessary that our pod design is above the isentropic limit for subsonic operation or above the Kantrowitz limit for supersonic operations (order of magnitude of meters):

$$Kn = \frac{k_b T}{\sqrt{2} \pi d^2 P l} \quad (1)$$

The characteristic length was set to a representative chord length of 1 m, temperature of 300 K, operating static pressures of 100 to 50 kPa and the hard diameter of O_2 (d) to 4.07×10^{-10} m [12]. This results in a minimum Knudsen number of 1.6×10^{-5} . From this, we can conclude that the continuum approach is suitable to solve the flowfield around the vehicle because the mean free path of molecules

is much smaller than the vehicle size. Furthermore, Pekardan and Alexeenko [13] proved that, for low-Mach-number flows, rarefaction effects due to localized gradients are not dominant, in contrast to full-scale Hyperloop designs. To evaluate the pod performance in a one-dimensional (1-D) manner, the Mach number distribution around the pod is based on the calculation of the area contraction between the inlet area and the space between the tunnel wall and the pod. Once this area contraction is known, the isentropic mass conservation equation is used to estimate the local Mach number:

$$\dot{m} = \frac{P_0}{\sqrt{RT_0}} A \sqrt{\gamma} M \left(1 + \frac{\gamma-1}{2} M^2 \right)^{(\gamma+1)/(2-2\gamma)} \quad (2)$$

We can then calculate the pressure gradient along the streamwise direction of the pod. To account for viscous effects, we estimate the laminar compressible boundary layer developing along the surface of the pod with the method proposed by Cohen and Reshotko [14]. This method solves the Karman boundary layer based on a tabulated shear parameter and correction factor [15] for arbitrary pressure gradients. Finally, we can estimate the friction coefficient C_f along the walls and the boundary-layer displacement thickness:

$$C_f \sqrt{Re_w} = 2S_p \sqrt{-\frac{(x/U_e)(dU_e/dx)}{n(T_e/T_0)}} = 2S_p \sqrt{-\frac{(x/l)P'(T_e/T_0)}{n}} \quad (3)$$

Before the design procedure, we verified the accuracy of this method against two-dimensional Navier–Stokes solutions with the commercial solver CFD++ developed by Metacomp Technologies [16]. Figure 4a depicts the 2-D pod shape for validation purposes where we used a traveling speed of $M_{\text{pod}} = 0.5$. Figure 4b plots the isentropic Mach number distribution along the upper surface of the pod. Initially, the flow accelerates up to the throat, reaching a Mach

number of 0.65, and from then on, the flow decelerates, imposing an unfavorable pressure gradient to the boundary layer. With the calculated pressure distribution along the wall, the shear stresses were retrieved via Eq. (3) and compared with the Navier–Stokes results (Fig. 4c). Because the shear stress is always above zero, we can conclude that no boundary-layer separation occurred before it reached the trailing edge. In case of an early boundary-layer separation, the drag rises rapidly, which should be avoided and taken into account during the design phase.

The reduced model allows a calculation of the lift from the isentropic Mach number distribution as well as of the drag viscous drag through the boundary-layer prediction. Hence, any pod shape could be analyzed in terms of its nondimensional aerodynamic characteristics (C_l and C_d based on the frontal area of the pod) in a timely manner. For longer pods, the boundary-layer code also predicts the displacement thickness, which could be implemented within the code to correct for the growth of the boundary layer along the pod.

At backpressures below 1 kPa, the critical Reynolds number was below $5 \cdot 10^5$ (based on the chord), which would suggest a laminar approach. However, at higher pressures and longer vehicles, a turbulent boundary-layer approach such as Stratford and Beavers [17] is proposed.

2. Two- and Three-Dimensional Assessment of the Pod with Computational Fluid Dynamics

Figure 5 depicts the 2-D domain bounded by the walls of the tunnel and the inlet plane, which was placed at least one chord length upstream of the pod and two chord lengths downstream to avoid any disturbance of the pod into the imposed boundary conditions. The surface of the pod was considered as an adiabatic no-slip wall, and the tube walls were assumed to be stationary slip walls. For this work, laminar simulations were considered for pressures below 1 kPa. However, for higher backpressures, the

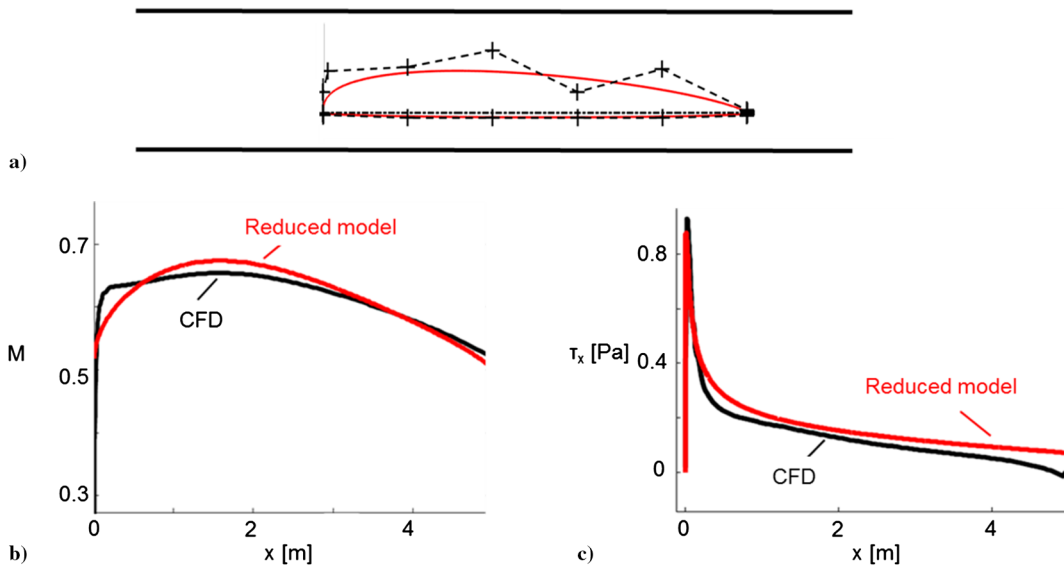


Fig. 4 Verification of the 1-D flow solution with CFD (CFD++): a) isentropic Mach number distribution, and b) wall shear stress on the upper wall of the pod along the streamwise direction.

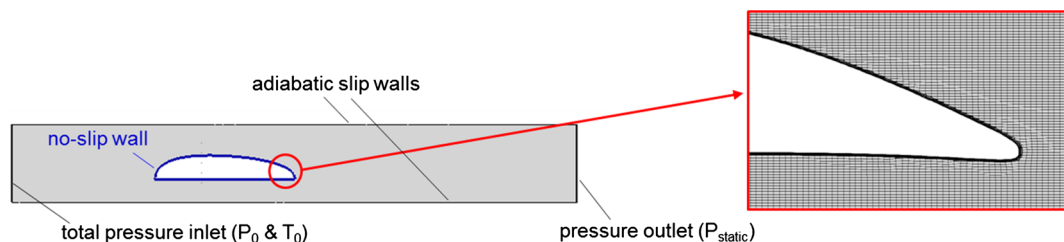


Fig. 5 Numerical domain of the 2-D simulations with a detailed zoom on the mesh.

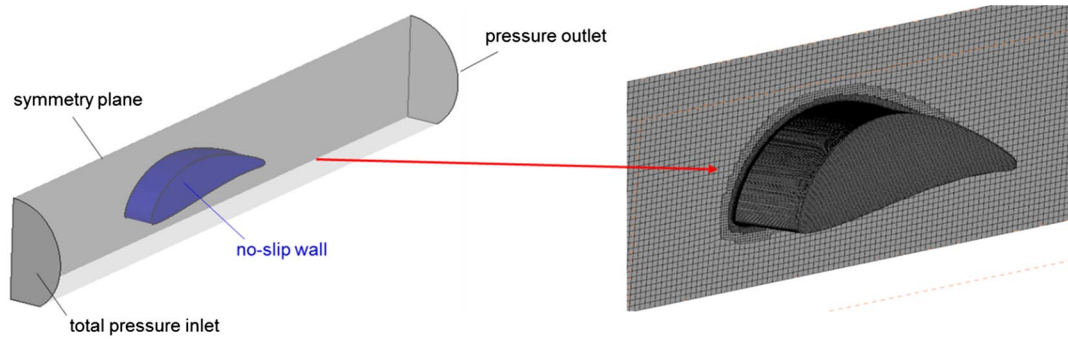


Fig. 6 Numerical domain of the 3-D simulations with a detailed zoom on the mesh.

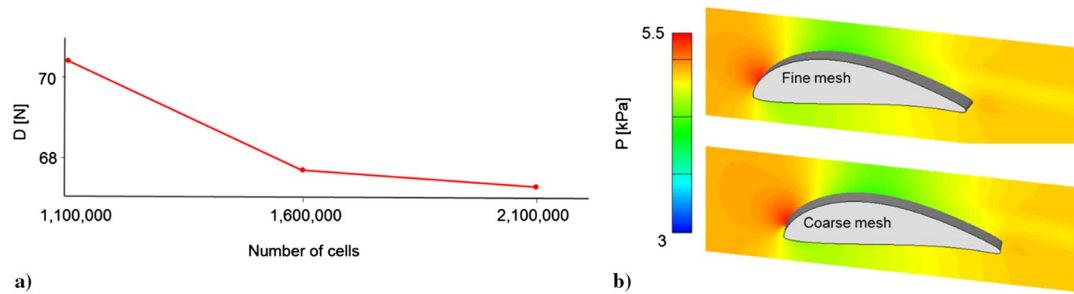


Fig. 7 Mesh sensitivity analysis: a) drag force on the pod in function for the coarse, medium, and fine grids; and b) isopressure contours of the pod for the fine and coarse meshes.

turbulence closure of the Reynolds-averaged Navier–Stokes (RANS) equations was provided by the $k - \omega$ shear-stress transport model [18]. Because no transition model was used, a turbulent boundary layer is computed from the stagnation point. In this case, an unstructured mesh was generated with the commercial software Hexpress[§]. We refined the discretization close to the pod's surface to keep the y^+ value below 1 and to ensure a correct prediction of the viscous sublayer. We used a total pressure inlet where a total pressure and total temperature are imposed in the inlet plane, based on a Mach number of 0.3 and a static temperature of 300 K. We set a backpressure boundary condition at the outlet plane equal to the freestream pressure.

A similar approach was used for the 3-D simulations. All the 3-D computations in this work had a numerical discretization with approximately 1.6 million grid points. In every simulation, the expansion ratio within the boundary layer is 1.4, whereas y^+ max is kept below 1 for all generated numerical domains. The computational domain is depicted in Fig. 6a, where a symmetry boundary condition was used to reduce the computational burden. The tube geometry was modeled after the one found in the Hyperloop competition rules and was modeled as a slip wall.

A mesh sensitivity study was carried out on a selected 3-D case (Fig. 6) according to the grid convergence index method as described by Celik et al. [19]. Three different meshes were designed: a coarse, medium and fine mesh of 1,100,000 elements, 1,600,000 elements and 2,100,000 elements respectively. The drag force on the pod was chosen as the representative variable; hence, Fig. 7a plots the drag value for the coarse, medium and fine grid for the coarse, medium, and fine grids, whereas Fig. 7b plots the isocontours of static pressure within the tube for the fine and coarse mesh. Numerical uncertainty on the fine mesh was 0.5%, and the extrapolated error from the medium to the fine mesh is less than 1% (based on the Richardson extrapolation [19,20]). Because of the low uncertainty and the lower computational burden, the settings of the medium mesh are selected for the 3-D calculations.

C. Optimization Routine

To optimize for a certain objective function (e.g., minimum drag), the geometrical parameterization and the evaluation routine are implemented into the flowchart depicted in Fig. 8. Typically, Mach number, inlet pressure, and temperature are known at the inlet. The design space (minimum and maximum height of the control points, length of the pod, etc.) was decided based on a preliminary parametric study set by the reduced-flow model. This model (described in Sec. II.B.1) calculates within a few seconds the aerodynamic quantities of interest (e.g., drag and lift) and inspired us to take advantage of the wall proximity to enhance lift. The first step is the geometry generation as described in Sec. II.A. This geometry passes through a constraint checker to inspect that the minimum pod height and minimum volume of the pod are met. The mesh is generated through a journal file [in this case via Hexpress (see footnote §)], and finally the geometry is calculated with CFD++ and postprocessed through Tecplot and CFD++. The routine is coupled with a differential evolution multi-objective optimizer, [21,22]. The two objectives are lift and drag. The evaluation routine of a single profile was approximately 4 min, which allowed to explore a wide range of design spaces and select an optimal one. Finally, a 3-D computational domain is generated for some of the selected geometries to compute the flowfield (Sec. II.B.2) to postprocess the quantities of interest such as lift and drag.

III. Results

A. Aerodynamic Enhancement Through the Tunnel Effect

1. Two-Dimensional Multi-Objective Optimization

Race cars generate a significant downforce through the suction effect between the front wing of the car and the road. Based upon that principle, we investigated the possible use of aerodynamic lift of the pod to reduce the power required from the air bearings or magnetic levitation with our optimization routine. The final shape of the pod is obtained by performing the optimization routine explained in Sec. II.C, with a fixed axial chord of 2.5 m. As shown in Fig. 9a, the flow accelerates over the suction side of the pod and decelerates over the pressure side, which generates the necessary lift. When moved closer to the upper wall (Fig. 9b top), the flow over-accelerates over the suction side up to the throat area and the following flow deceleration

[§]Data available online at <http://www.numeca-usa.com/en> [retrieved 20 February 2017].

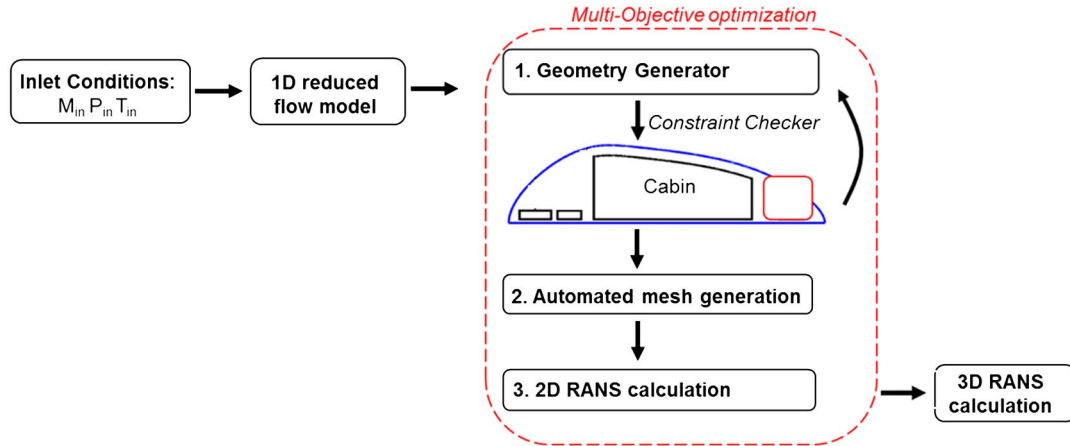


Fig. 8 Optimization strategy.

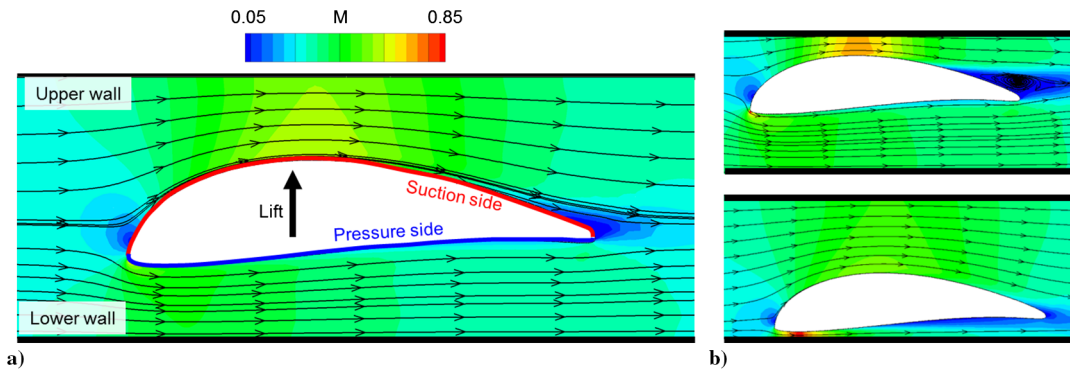


Fig. 9 Lifting-body concept: tunnel effect.

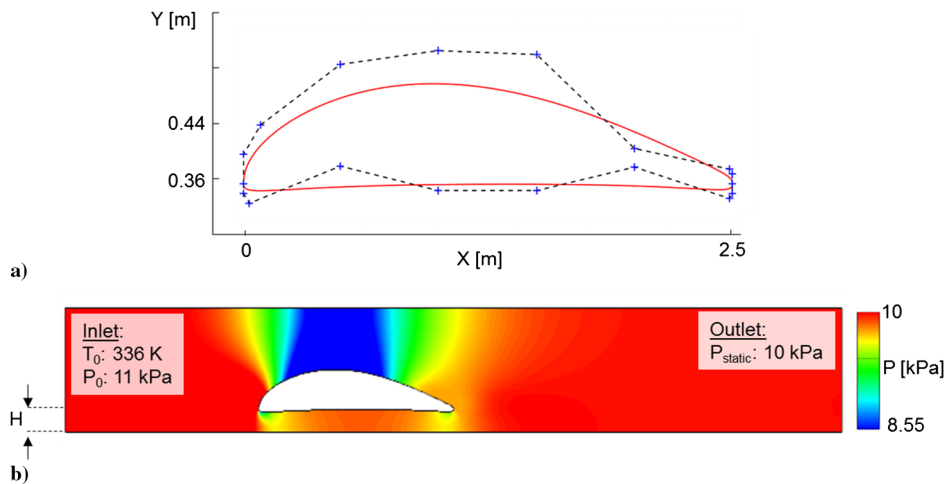


Fig. 10 Representations of a) Bezier parameterization for initial design, and b) numerical domain for the optimization.

could lead to an earlier boundary layer separation, augmenting drag and decreasing the lift. When moved closer to the lower wall (Fig. 9b down), the pressure side can be optimized to explore the presence of the lower wall and build additional pressure to enhance lift. Hence, the combined effect of the upper and lower walls will lead to an optimal pod height.

Figure 10a depicts the selected parameterization where the leading- and trailing-edge Bezier points were fixed for this optimization; however, the middle points were free to move in the vertical direction, with minimum and maximum values fixed by the 1-D design. Figure 10b shows the numerical domain, and H represents the distance between the leading edge of the pod and the bottom wall, which was set as a free parameter. The total amount of free parameters was nine. The optimization was performed for an inlet condition of 10 kPa static

pressure and an inlet velocity of 110 m/s, which corresponded to an inlet total pressure of 11 kPa and a total temperature of 336 K.

The results of the optimization are shown in Fig. 11; 605 profiles were calculated and optimized for lift and drag. The design of experiments profiles (DOE, 128 profiles) are depicted in gray, whereas the first populations are depicted in light blue and the last eight populations of the optimization in dark blue. When investigating a profile from the DOE (individual 69), relatively flat pressure side profiles are observed. However, throughout the optimization, the pressure side as well as the suction side are more shaped as a wing design to maximize lift and minimize drag (observed when moving from individual 69 from the DOE, to individual 16 of the first population (POP. 1) to individual 16 of the 10th population (POP. 10)). Interestingly, at the Pareto front, the drag

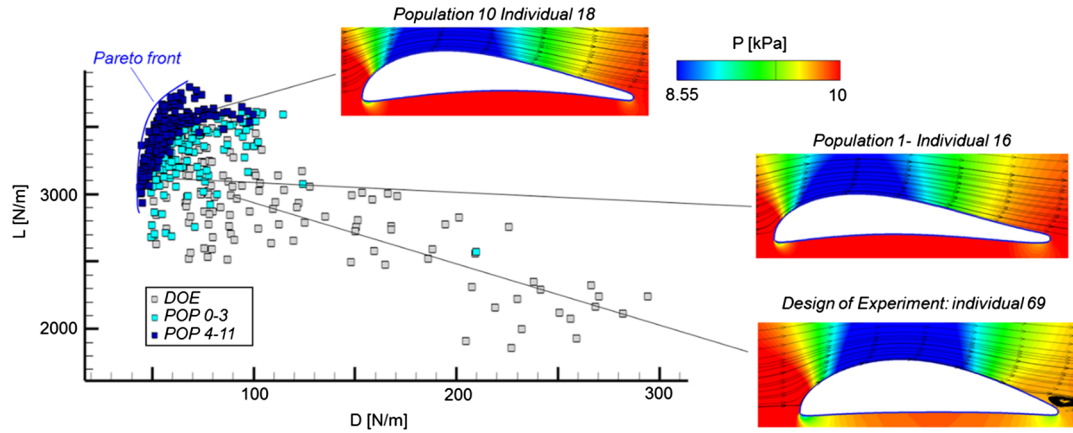


Fig. 11 Pareto front of the multi-objective optimization with three selected profiles.

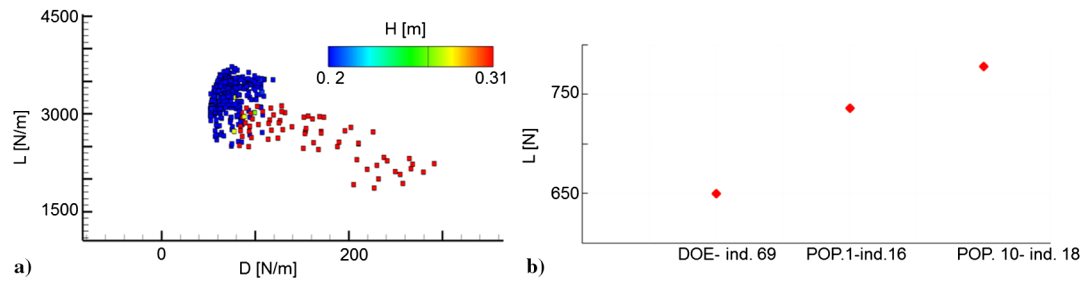


Fig. 12 Representations of a) optimal height in function of the lift coefficient for all the investigated 2-D geometries, and b) comparison of the lift for three designs with 3-D RANS simulations.

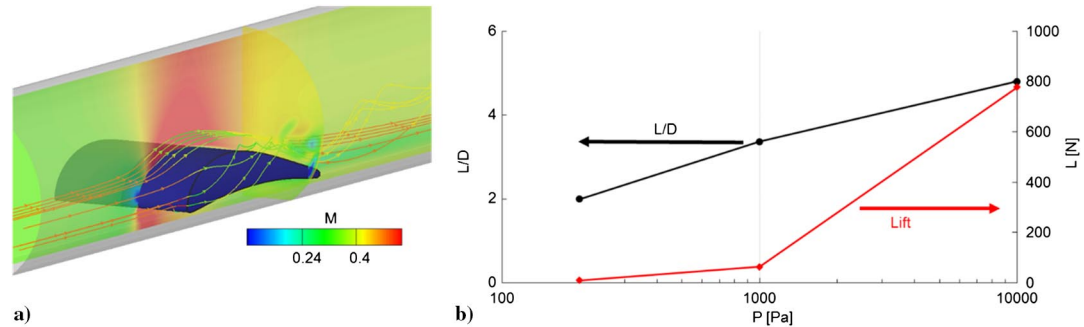


Fig. 13 Representations of a) 3-D Mach contour of the optimized geometry for the lifting-body concept, and b) log-linear scale of lift and L/D in function of the operating pressure for the 3-D assessment.

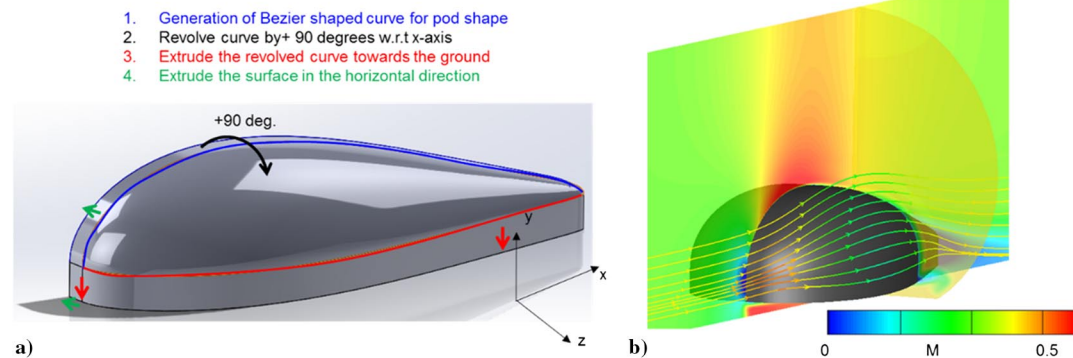


Fig. 14 Representations of a) design methodology for the minimum-drag concept, and b) 3-D Mach contour of the optimized geometry for the minimum-drag concept.

has much smaller variations when compared to the lift. Finally, the shape of individual 18 from population 10 was chosen as the optimal value because it lays within the optimal L/D values.

In Fig. 12a, each individual is colored according to the height (H) of the pod. We can observe that all optimized designs move toward

$H = 0.2$ m, which represents 13% of the tunnel height. Although the optimizer shapes the pressure and suction side of the pod according to the presence of the tunnel, the optimizer tends to favor the bottom of tunnel to build additional pressure on the pressure side. The three designs depicted in Fig. 11 were extruded and analyzed with 3-D

Table 1 Lift and drag values for the 3-D case for the initial and optimized shapes

Parameter	Initial shape (DOE individual 69)	Maximum-lift design (extruded)	Minimum-drag design (revolved)
L , N	650	778	−20
D , N	180	162	51
L/D	3.6	4.8	−0.4

RANS simulations and compared for their lift. The 3-D design was based on an extruded 2-D profile with an extruded length of 1.4 m. From Fig. 12b, it is observed that individual 69 from the DOE has the lowest lift, as predicted by the 2-D optimization and that individual 18 from population 10 outperforms the DOE by 20%, confirming the superior design by the multi-objective optimization.

2. Three-Dimensional Flow Features

The optimized 3-D design with a volume of 0.9 m³ was based on the optimized 2-D profile and is visualized in Fig. 13a. Figure 13b shows lift L and L/D values for several operating conditions. Lift increases from 10 N at operating pressure of 200 Pa to 778 N at 10 kPa. L/D increases from 2 until 4.8 at 10 kPa but was lower than the 2-D prediction. This can be explained based on the fact that the 2-D design was performed at midspan of the pod, however, in 3-D, as we move closer to the lateral walls, the distance between the pod and the tunnel changes and 3-D flow features are predominant. In particular, vortices appear due to the pressure gradient between the suction and pressure side of the pod (seen in Fig. 13a). As a consequence, the pressure difference between the lower and upper part of the pod decreased.

B. Aerodynamic Enhancement Through a Minimum-Drag Design

To generate a low-drag vehicle, a dedicated geometrical 3-D parameterization was applied because the 3-D design method for the lifting body faced limited control in terms of 3-D shaping. As exemplified in Fig. 14a, 2-D suction side profile obtained from the multi-objective optimization for lift and drag. We revolved the 2-D Bezier profile by 90 deg in each direction, which delivers a wider 3-D control while keeping the design parameters to a minimum. This step allows to taper the back of the pod, which augments the flow guidance, consequently reducing the wake size and the generation of vortices observed in the high-lift vehicle. The third step is the extrusion of this revolved volume toward the ground (in this case, the negative y axis) and fourth to extrude the revolved surface toward the center (z axis) if the volume of the pod is not sufficient to accommodate for all system constraints, as described in Sec. II.A. For our study, the pod is extruded toward the bottom by 0.15 m and by 0.1 m toward the z axis such that all vehicles share the same volume. Figure 14b depicts the Mach number for the pod at an operating condition of 10 kPa at a speed of 110 m/s, with a drag reduction of 69% compared to the maximum-lift design. We observe that the streamlines follow the pod surface in an aerodynamic way and only identified a small vortex generation close to the bottom part due to the high-pressure gradient in this zone.

Table 1 summarizes the lift and drag values of the initial shape (based on the extruded profile of individual 69 of the DOE) compared to the maximum-lift design and the minimum-drag design. For the minimum-drag design, the tunnel effect provided negative lift values with an L/D of −0.4.

IV. Conclusions

In the present paper, an aerodynamic design procedure of the Hyperloop vehicle was proposed and developed. The design process started with a parameterization of the geometry with the consequent preliminary quasi-1-D analysis of the flowfield around the pod through a reduced-flow model. Special care was taken to prevent choking of the flow at the throat of the pod as well as separation at the rear part of the vehicle. The design was optimized

via a differential evolution multi-objective optimizer coupled to a 2-D RANS solver, and results were compared to 3-D RANS simulations. During the design process, several aerodynamic design objectives were evaluated to explore different conceptual ideas. One of the objectives focused on the ability to generate a certain amount of lift to mitigate the responsibility of the main levitation process. 3-D simulations revealed an increase of 20% of lift compared to the baseline design and an L/D of 4.8, which was lower than the 2-D prediction due to the generation of tip vortices. Another design philosophy targeted the minimization of the aerodynamic drag generated by the pod. Through a particular 3-D parameterization, it was possible to reduce the drag by 69% when compared to the optimized maximum-lift design. Future efforts will target the use of 3-D parameterization to perform a full 3-D optimization analysis based on the 2-D optimization.

Acknowledgments

The authors would like to thank Alina Alexeenko from Purdue University for her valuable input as well as Guillermo Paniagua from Purdue University. Furthermore, we would like to acknowledge the Purdue Hyperloop team, in particular Bill O'Neill. We would also like to thank Noemie Guerin, Val Joiner and Zhe Liu of Purdue University for their help with the revision of this paper.

References

- [1] Musk, E., "Hyperloop Alpha," SpaceX, Hawthorne, CA, 2013, http://www.spacex.com/sites/spacex/files/hyperloop_alpha.pdf [retrieved 20 Feb. 2017].
- [2] Nielsen, E. J., and Anderson, W. K., "Recent Improvements in Aerodynamic Design Optimization on Unstructured Meshes," *AIAA Journal*, Vol. 40, No. 6, 2002, pp. 1155–1163. doi:10.2514/2.1765
- [3] Torres Gabriel, E., and Mueller Thomas, J., "Low Aspect Ratio Wing Aerodynamics at Low Reynolds Numbers," *AIAA Journal*, Vol. 42, No. 5, 2004, pp. 865–873. doi:10.2514/1.439
- [4] Chen, X., Zho, L., Ma, J., and Liu, Y., "Aerodynamic Simulation of Evacuated Tube Maglev Trains with Different Streamlined Designs," *Journal of Modern Transportation*, Vol. 2, No. 2, 2012, pp. 115–120. doi:10.1007/BF03325788
- [5] Chin, J. C., Gray, J. S., Jones, S. M., and Berton, J. J., "Open-Source Conceptual Sizing Models for the Hyperloop Passenger Pod," *56th AIAA/ASCE/AHS/ASC Structures, Structural Dynamics, and Materials Conference*, AIAA Paper 2015-1587, Jan. 2015. doi:10.2514/6.2015-1587
- [6] Decker, K., Chin, J., Peng, A., Summers, C., Nyguen, G., Oberlander, A., Sakib, G., Sharifrazi, N., Heath, C., Gray, J., and Falck, R., "Conceptual Feasibility Study of the Hyperloop Vehicle for Next-Generation Transport," *55th AIAA Aerospace Sciences Meeting*, AIAA Paper 2017-0221, Jan. 2017. doi:10.2514/6.2017-0221
- [7] Taylor, C., Hyde, D., and Barr, L., "Hyperloop Commercial Feasibility Analysis," U.S. Dept. of Transportation, TR DOT-VNTSC-NASA-16-01, Cambridge, MA, 2016.
- [8] Hyperloop Competition, SpaceX, Hawthorne, CA, <http://www.spacex.com/hyperloop> [retrieved 20 Feb. 2017]
- [9] "MIT Engineers Win Hyperloop Pod Competition, Will Test Prototype in Mid-2016," Newatlas, Bangkok, Thailand, Jan. 2016, <http://newatlas.com/mit-hyperloop-competition/41589> [retrieved 20 Feb. 2017].
- [10] Kantrowitz, A., and Donaldson, C., "Preliminary Investigation of Supersonic Diffusers," NACA Rept. WR-L-713, 1945.
- [11] Sousa, J., and Paniagua, G., "Entropy Minimization Design Approach of Supersonic Internal Passages," *Entropy*, Vol. 17, No. 8, 2015, pp. 5593–5610. doi:10.3390/e17085593
- [12] Bird, G. A., "Molecular Gas Dynamics," NASA TR A76, 1976.
- [13] Pekardan, C., and Alexeenko, A., "Rarefaction Effects for the Transonic Airfoils in Low Reynolds Number Regime," *46th AIAA Thermophysics Conference*, AIAA Paper 2016-4429, June 2016. doi:10.2514/6.2016-4429
- [14] Cohen, C. B., and Reshotko, E., "The Compressible Laminar Boundary Layer with Heat Transfer and Arbitrary Pressure Gradient," NACA Rept. TR-1294, 1956.

- [15] Ness, N., "Some Comments on the Laminar Compressible Boundary-Layer Analysis with Arbitrary Pressure Gradient," *AIAA Journal*, Vol. 5, No. 2, 1967, pp. 330–331.
doi:10.2514/3.3961
- [16] Chakravarthy, S., Peroomian, O., Goldberg, U., and Palaniswamy, S., "The CFD++ Computational Fluid Dynamics Software Suite," SAE Technical Paper 985564, 1998.
doi:10.4271/985564
- [17] Stratford, B. S., and Beavers, G. S., "The Calculation of the Compressible Turbulent Boundary Layer in an Arbitrary Pressure Gradient: A Correlation of Certain Previous Methods," Her Majesty's Stationery Office, ARC/R&M-3207, London, U.K., 1961.
- [18] Menter, F. R., "Two-Equation Eddy-Viscosity Turbulence Models for Engineering Applications," *AIAA Journal*, Vol. 32, No. 8, 1994, pp. 1598–1605.
doi:10.2514/3.12149
- [19] Celik, I. B., Ghia, U., and Roache, P. J., "Procedure for Estimation and Reporting of Uncertainty Due to Discretization in CFD Applications," *Journal of Fluids Engineering-Transactions of the ASME*, Vol. 130, No. 7, 2008, pp. 1–14.
- [20] Bonfiglioli, A., and Paciorri, R., "Convergence Analysis of Shock-Capturing and Shock-Fitting Solutions on Unstructured Grids," *AIAA Journal*, Vol. 52, No. 7, 2014, pp. 1404–1416.
doi:10.2514/1.J052567
- [21] Verstraete, T., Amaral, S., Van den Braembussche, R., and Arts, T., "Design and Optimization of the Internal Cooling Channels of a HP Turbine Blade: Part 2—Optimization," *Proceedings of the ASME Turbo Expo: Power for Land, Sea, and Air, Volume 4: Heat Transfer, Parts A and B*, 2008, pp. 977–987.
doi:10.1115/GT2008-51080
- [22] Verstraete, T. T., Alsalihi, Z. Z., and Van den Braembussche, R. A., "Multidisciplinary Optimization of a Radial Compressor for Microgas Turbine Applications," *ASME Journal of Turbomachinery*, Vol. 132, No. 3, 2010, Paper 031004.
doi:10.1115/1.3144162

J. Poggie
Associate Editor